Aerodynamic study of a Hyperloop pod equipped with compressor to overcome the Kantrowitz limit

Author(s):
Bizzozero, Maurice; Sato, Yohei; Sayed, Mohamed

Publication date:
2021-11

Permanent link:
https://doi.org/10.3929/ethz-b-000510226

Originally published in:
Journal of Wind Engineering and Industrial Aerodynamics 218, https://doi.org/10.1016/j.jweia.2021.104784

Journal of Wind Engineering & Industrial Aerodynamics 218 (2021) 104784

Contents lists available at ScienceDirect

Journal of Wind Engineering & Industrial Aerodynamics

journal homepage: www.elsevier.com/locate/jweia

Aerodynamic study of a Hyperloop pod equipped with compressor to overcome the Kantrowitz limit

Maurice Bizzozero [a,b], Yohei Sato [b,*], Mohamed Aly Sayed [b,c]

[a] Department of Mechanical and Process Engineering, Swiss Federal Institute of Technology, ETH Zürich, Rämistrasse 101, 8092 Zürich, Switzerland
[b] Division of Scientific Computing, Theory and Data, Paul Scherrer Institute, Forschungsstrasse 111, 5232 Villigen, Switzerland
[c] Swiss Federal Institute of Technology, EPFL Lausanne, Route Cantonale, 2015 Lausanne, Switzerland

ARTICLE INFO

Keywords:
CFD
Hyperloop
Kantrowitz limit
Compressor modeling
Aerodynamic drag

ABSTRACT

This paper describes an investigation of the aerodynamic performance of a Hyperloop pod equipped with an axial compressor using CFD simulation. The compressor is expected to reduce the drag if the operational speed of the pod exceeds the Kantrowitz Limit (KL). To evaluate the effectiveness of the compressor, two types of pod have been designed: those with and those without a compressor. A validation study was undertaken for supersonic flow around a cylindrical body in a wind tunnel. Several combinations of pod Mach number and blockage ratios were examined. The axial compressor was modeled with the fan interface model and our original method, which we call the source terms model. Results are similar, but our model has the advantage that it can be applied to higher pressure ratios without inducing numerical instabilities. The power consumption was reduced owing to the compressor by decreasing the pressure accumulated in front of the pod. The effectiveness of the compressor was shown to be greater for conditions well above the KL, with a maximum power reduction of 47.5%. Simulations performed half-scale, and at a different system pressure, showed that the effectiveness of the compressor was not greatly influenced by these parameters.

1. Introduction

Climate change is one of the greatest challenges humanity has ever faced. The transportation sector accounts for about one fifth of the total CO_2 emissions, the main contributor to the greenhouse effect (Eurostat (European Commission), 2013). Additionally, the global travel network and the need for mobility are growing. A study on future mobility shows that the demand of fast-speed travel is increasing (Schafer and Victor, 2000). It is forecast that 41% of the world market share will belong to high-speed transport by 2050. Evacuated tube train system, in which vacuum pumps extract the air in the tube in order to reduce the aerodynamic drag of the train, is considered to be one of the solutions to meet the demand of high-speed transport with low CO_2 emissions.

Over the last few decades, the concept of vacuum tube transportation has been investigated multiple times. The first concept was proposed in the beginning of the 20th century by the rocket pioneer Robert H. Goddard. In 1972, the Rand Corporation published a series of papers regarding a detailed underground tube system, called the "Very High Speed Transit System", which was supposed to connect Los Angeles to New York with few other stops (Salter, 1972). A similar idea was proposed in Switzerland in the late 1970s. A national project, called Swissmetro, included an underground vacuum tunnel system for high speed magnetic levitating passenger trains (Jufer et al., 1993). However, none of these projects ever came to fruition. The concept of high-speed transportation has regained attention in the recent years mostly due to the Hyperloop pod competition held by Elon Musk, in which a number of student and non-student teams participated (Space Exploration Technologies Corp., 2015). The Hyperloop alpha system proposed by Musk (Musk, 2013), similarly to his predecessors, consists of a low pressure tube (100–10000 Pa) with capsules traveling at high subsonic speed ($Ma = 0.99$) using aerostatic levitation. Here Ma indicates the Mach number. The transport system was proposed as an alternative to the California high-speed rail (https://www.hsr.ca.gov/) connecting San Francisco and Los Angeles.

The feasibility of Hyperloop alpha was discussed in the paper (Musk, 2013), but NASA also conducted feasibility studies (Chin et al., 2015; Hyde et al., 2016; Decker et al., 2017) with respect to the commercial potential, environmental impact, costs, safety issues, and regulatory and policy issues, as well as the technological issues. In this paper, our focus is put on one of the most important technological issues: the so-called Kantrowitz limit.

In contrary to open systems such as high speed conventional trains, the flow around a pod in a closed tube has different aerodynamic

* Corresponding author.
E-mail address: yohei.sato@psi.ch (Y. Sato).

https://doi.org/10.1016/j.jweia.2021.104784
Received 8 June 2021; Received in revised form 7 September 2021; Accepted 20 September 2021
Available online 7 October 2021

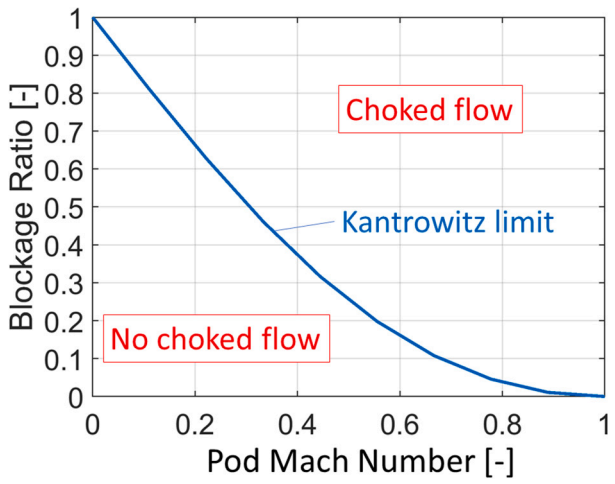

Fig. 1. The Kantrowitz limit defined by Eq. (1).

features. In case of open systems, shock waves appears when a vehicle travels at the speed of sound, meanwhile a vehicle in a tube faces shocks at lower traveling speed due to bypass flow acceleration in the converging part between the tube and the vehicle (Musk, 2013).

1.1. The Kantrowitz limit

For given the pod and tube sizes, there is a maximum pod speed after which the flow around the pod (in the bypass) chokes. This sonic condition is known as the Kantrowitz Limit (KL) (Kantrowitz and Donaldson, 1945). By defining the blockage ratio (BR) as $BR = A_{pod}/A_t$ (with A_{pod} as the pod cross-sectional area and A_t as the tube cross-sectional area), the KL relates the pod Mach number Ma and the BR as follows:

$$BR = 1 - Ma\left(\frac{1+\frac{\gamma-1}{2}}{1+\frac{\gamma-1}{2}Ma^2}\right)^{\frac{\gamma+1}{2(\gamma-1)}}, \quad (1)$$

where Ma = pod advance speed / speed of sound, and γ is the heat capacity ratio, e.g. $\gamma = 1.4$ for air at standard conditions.

As plotted in Fig. 1, for conditions above it (i.e. higher Mach numbers and/or larger blockage ratios) the flow around the pod is choked. Once chocked condition is reached, the pod starts behaving like a piston causing a substantial increase of adverse pressure. This is also referred to as the syringe effect. A higher adverse pressure results in an increased drag and ultimately higher power required to propel the pod. Thus, exceeding the KL can be detrimental for the performance of the system and should be mitigated. Increasing the tube size and thus reducing the blockage ratio is not ideal since it would increase the costs and make the system less feasible. An alternative solution is the implementation of an axial compressor in the fore part of the pod that would allow more throughput by releasing part of the accumulated pressure upstream of the pod (Musk, 2013).

1.2. Previous studies

Research on partially evacuated tube trains has, in the recent years, focused on the aerodynamic drag and the influence of the most relevant parameters. Kim et al. (2011) investigated the effects of varying internal-tube pressure, blockage ratio and operating speed by using CFD analysis for a symmetric elongated vehicle. Relations among those parameters were calculated to obtain the same energy efficiency of open field trains. Similarly, Zhang (2012) also performed axisymmetric CFD simulations of a train traveling at different speeds under different pressures and with different blockage ratios. They concluded that BR, tube internal diameter and vacuum pressure should be within specific ranges for the feasibility of the system. The axisymmetric CFD simulations were also performed by Zhou et al. (2019), in which the dynamic adaptive mesh method was incorporated to capture the shock waves. Oh et al. (2019) included the pod length and tube temperature in the analysis, and concluded that increasing the tube temperature can delay the onset of choking and slightly reduce the aerodynamic drag. Moreover, they observed that increasing the blockage ratio significantly affects the pressure drag, while as the pod speed increased, strong shock waves occurred near the end of the pod. Kang et al. (2017) extended the study with 3D simulations and observed that by increasing the pod speed, the drag coefficient becomes maximum near the Kantrowitz limit and then decreases, showing the typical transonic flow pattern. The pattern of the drag coefficient according to the pod Mach number of the 3D simulations was compatible with that of axisymmetric ones. The system pressure also predictably influences the drag. Since the largest contribution to the drag is pressure drag, a quasi-linear relation is observed (Wang et al., 2017). The pod front shape does not have a significant influence on the total drag (Chen et al., 2012).

In parallel to the investigations on the drag of the pod/train, pod design procedures have been proposed. Braun et al. (2017) reported the aerodynamic design procedure applied to their pods for conditions below the KL. A multi-objective optimization coupled with axisymmetric two-dimensional CFD simulations is used to obtain an optimal pod shape for two distinct goals; maximizing the lift and reducing the drag. The optimized design with the first objective showed an increase in lift of 20% compared to the baseline design, while the second optimization lead to a 69% reduction in drag. Opgenoord and Caplan (2017) presented an optimization procedure of the pod developed by the Hyperloop competition team of the Massachusetts Institute of Technology (MIT). Even though their pod was designed to travel at conditions below the Kantrowitz limit (Ma 0.3 and blockage ratio 0.3), the study included the region above the Nick and Sato (2020) optimized the shape of the pod developed by the Hyperloop competition team of the Eidgenössische Technische Hochschule (ETH) of Zürich. The gamma transition model was used to accurately predict the laminar–turbulent flow transition. The total drag for the optimized design was 14% smaller than the initial one. Wong (2018) investigated the aerodynamic characteristics of the Hyperloop pod, with the objective of finding a pod shape that minimizes the total drag. The author concluded that, for a fixed blockage ratio, a blunt nose and a streamlined tail are key features which allowed to reduce the total drag by 11%.

The formation and development of shock waves has been a topic of interest. Niu et al. (2019) analyzed the effects of shocks on the temperature and pressure fields in the proximity of the pod and tube walls. The authors concluded that shock waves could endanger the structural safety of the pod and affect the normal operation of equipment in the vehicle and tube. Sui et al. (2020) investigated how the aerothermal environment in the tube is influenced by the blockage ratio. It was found that the latter can contribute to the deterioration of such environment, since it affects the strength of the shock waves around the pod. Le et al. (2020) studied the pressure waves propagation upstream and downstream of the pod. It was observed that the compression wave in the upstream region travels faster than the speed of sound, while the expansion wave in the downstream region prolongates at the speed of sound. The aerodynamic behavior of the Hyperloop pod with an axial channel (i.e. a duct through the centerline of the pod) and a radial gap (i.e. a cut between fore and rear part of the pod, such as between train wagons) was also studied (Zhou et al., 2021). Both inclusions affect the wake of the pod and can reduce the high temperatures caused by a shock wave when the KL is exceeded. An investigation of the effects of a cross passage shows that the passage can improve the aerodynamic characteristics in the case of a single train passing, but aggravate the aero-thermal environment in the case of two trains crossing (Hu et al., 2021).

Few studies focused on the mitigation of the Kantrowitz limit. Bose and Viswanathan (2021) investigated the possibility of alleviating this effect using passive flow control. This was done through mounting an arrangement of airfoils on the pod body. The results show that the addition of fins helps in reducing the drag and provide a positive lift to the pod. However, the solution proposed in the original formulation in the alpha paper, the compressor, has not been studied with sufficient depth yet. Recently, Lluesma-Rodríguez et al. (2021) performed a series of CFD simulations to investigate the effects of the axial compressor on the total power consumption of the pod. It was found that for high blockage ratios the power consumption can be reduced up to 70% with the addition of the compressor. Their study represents the first attempt to examine the potential benefits of a compressor by the means of CFD simulations. However, relatively few pod traveling conditions were tested and the operating conditions of the compressor were not investigated. The potential inclusion of a compressor in a Hyperloop pod still requires more detailed investigations.

This study aims to fill the gap in the literature and investigate the possibility of mounting an axial compressor in the fore part of the pod to mitigate the Kantrowitz limit. In this light, the present paper with two distinct pod designs is two-fold. In the first part, a pod without the compressor is simulated under different conditions (BR and pod Mach number), with focus on the flow structure and drag acting on the pod. This serves as motivation for the compressor investigation. In a second setup, a modeling of the compressor is included in the simulation and the effects on the flow are studied. The goal is to assess whether mounting a compressor is beneficial for the Hyperloop system in terms of overall power consumption.

This paper is organized as follows. The pod and tube designs are shown in Section 2. The numerical simulation is presented in Section 3. Section 4 describes the verification procedure. The results of the simulations are presented and discussed in Section 5. Finally, the conclusions are drawn in Section 6.

2. Pod and tube designs

The pods considered in this paper were non-levitating, driven by the thrust of the Linear Induction Motor (LIM) and the axial compressor when mounted. The effect of wheels supporting the pod was neglected to simplify the geometry for the CFD simulations. Two types of pod designs were designed: one without a compressor and one with a compressor. Fig. 2(a) shows the central cross section of the hull without a compressor. The hull is composed of ellipsoidal bodies for the front and rear parts connected to a cylindrical body in between. Each ellipse extends to 1/4 of the total pod length. The pod radius r_{pod} is the main design parameter which corresponds to the blockage ratio. The blockage ratio for the pod without compressor is defined as:

$$BR = \frac{\pi r_{pod}^2}{\pi r_{tube}^2}, \tag{2}$$

where r_{tube} is the tube radius, which was kept constant. The pod length is constrained by the ratio of body length to the radius, i.e. $L_{pod}/r_{pod} = 10$.

Fig. 2(b) shows the central cross section of the pod with a compressor. The duct in the pod with radius r_{duct} is designed to transfer the compressed air from the front to the rear side, which is similar to the design concept of Hyperloop alpha (Musk, 2013). The external radius of the pod r_{pod} is a design variable which corresponds to the blockage ratio. The blockage ratio for the pod with compressor is defined as:

$$BR = \frac{\pi(r_{pod}^2 - r_{duct}^2)}{\pi r_{tube}^2}. \tag{3}$$

The ratio L_{pod}/r_{pod} is constrained to be 10 as for the pod without a compressor. The area of the duct is constrained to be a fixed ratio of the frontal area of the pod, i.e. $A_{duct}/A_{pod} = 0.2$. The converging part of the duct extends to 1/4 of the pod length. The modeling of the compressor, discussed in Section 3.5 is located in the converging part, as indicated.

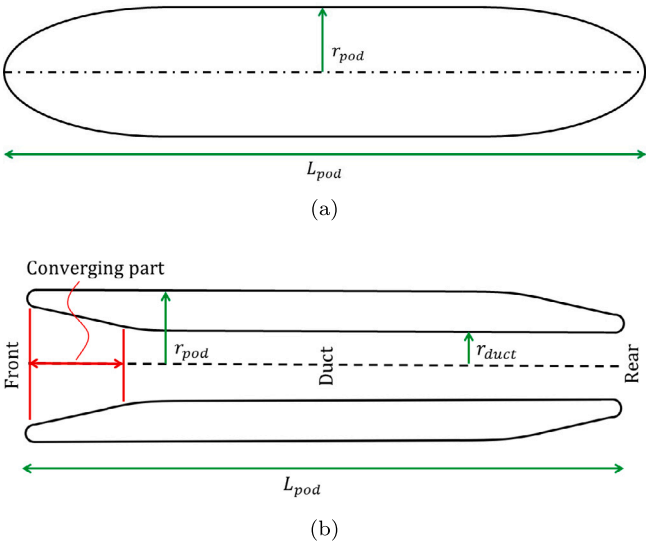

Fig. 2. Definition sketch of pod (a) without compressor and (b) with compressor.

The tube was designed as a cylinder with the diameter of 2.2 m, dimension that was taken from the facility of EuroTube (EuroTube Foundation, 2019). In reality, there is a floor at the bottom (Space Exploration Technologies Corp., 2015), and the inside shape of the tube is not cylindrical. However it was assumed to be cylindrical in the 2D axisymmetric CFD simulations for simplification.

3. Numerical simulation

3.1. Assumptions

The air inside the partially evacuated tube was assumed to be a continuum. The continuum hypothesis was evaluated by the Knudsen number $Kn = \lambda/L$, where λ is the molecular mean free path and L the characteristic length scale of the flow, which for this study is the diameter of the tube. The air pressure inside the tube was set to 1.0132×10^4 Pa for the analysis. For this condition, the Knudsen number is $Kn = \mathcal{O}(10^{-6})$, which is far below the limit value of $Kn = \mathcal{O}(10^{-3})$ and thus the continuum hypothesis was considered to be applicable (Chen, 2005).

The simulations were performed under the steady state assumption. This simplification does not allow to capture the shock wave propagation upstream and downstream of the pod (Le et al., 2020). However, the flow around the pod is not influenced by the shock propagation and thus the steady assumption can be still used (Zhang, 2012; Oh et al., 2019). The flow was assumed to be fully turbulent, therefore the influence of the transition from laminar to turbulent flow regime was neglected.

3.2. Governing equations and discretization

In this study, we used the commercial CFD software STAR-CCM+ (Siemens PLM. Software, 2020). The governing equations are the mass, momentum and energy equations for compressible flow under the assumption of the ideal gas law. The governing equations are discretized with the finite volume method in space. The inviscid flux was calculated by using Roe's flux-difference splitting scheme (Roe, 1986), while the second-order accurate scheme was used for the viscous fluxes. The coupled flow solver was used in which the implicit pseudo-time integration was employed.

Three turbulence models were used for validating the solver: the Spalart–Allmaras model, the realizable $k-\varepsilon$ model and the SST $k-\omega$ model with the two-layer all y^+ wall treatment (Siemens PLM. Software, 2020). Although the results of these three models did not show significant difference (as described in Section 4.3), the $k-\varepsilon$ model gave the best match with the experimental data, and hence it was used for all further simulations in Section 5.

3.3. Computational domain and boundary conditions

The computational domain for the two-dimensional axisymmetric case is illustrated in Fig. 3 together with the boundary conditions. Here, a representative case for a pod without a compressor is shown, but the same setup was used for the pod with a compressor. The tube radius was set to 1.1 m, which was taken from the one currently constructed by EuroTube (EuroTube Foundation, 2019). The domain ranges -10 m $\leq x \leq$ 30 m in the advancing direction with the origin located at the nose of the pod. For example, in case that $BR = 0.2$, $r_{pod} = 0.49$ m and $L_{pod} = 4.9$ m, which results in the downstream region length as approximately $5L_{pod}$.

The coordinate system is fixed to the pod and the outer wall moves towards the positive x-direction at the advance speed of the pod. The inlet boundary condition was set to mass flow inlet. The mass flow value was calculated based on the pod speed and density of air. The temperature of the air at the inlet was set to 300 K. A pressure outlet condition was adopted for the outlet boundary. The no slip wall boundary condition was assigned to the wall of the tube and the pod. The wall of the tube was translated to the positive x-direction at the same pod traveling speed.

3.4. Computational mesh

The computational mesh was generated with the automatic mesher implemented in STAR-CCM+. The combination of Prism Layer Mesher and Trimmer was used. Prism Layer Mesher makes thin quadrilateral meshes near the wall region, whereas Trimmer generates hexahedral elements in the bulk region. The prism layers consist of 20 layers with a stretching factor of 1.3 and a first cell thickness of 0.025 mm, which corresponds to $Y^+ \approx 1$. A mesh dependency study was performed as described in Section 4.1, and the resulting optimal mesh parameters were used for all the simulations reported in Section 5.

3.5. Compressor model

The aim of the compressor mounted on the fore part of the pod is to actively transfer high-pressure air from the front to the rear of the vessel through the center duct (Musk, 2013). Two distinct approaches were evaluated as the modeling of the compressor.

The first option available in STAR-CCM+ is the so-called fan interface model, which is developed for axial fans. In this model, the fan is represented by a zero-thickness interface with an imposed pressure jump across it, and the value of the pressure difference can be defined by the user (Siemens PLM. Software, 2020). In this study, the fan interface was positioned at the entry of the converging section, as shown in Fig. 4(a). The pressure increases across the interface as illustrated in Fig. 4(c), where p^* = absolute pressure (Pa) / p_{inf} (Pa), p_{inf} = 10'132 (Pa) and $X^* = X$ (m) / Pod length (m).

The second approach is the source terms model, which was newly developed by us and implemented through a user-defined function. Two source terms, momentum source and heat source, are added to the specified region of the fluid domain as depicted in Fig. 4(b). The momentum source S_m is defined as a volumetric body-force:

$$S_m = T_{compr}/V_{src}[\mathrm{N/m^3}], \tag{4}$$

where T_{compr} is the thrust of the compressor and V_{src} is the volume of the compressor. In order to achieve the isentropic condition across the compressor, the heat source was added to the energy equation. This source term was distributed uniformly in the same way as the momentum source term. The heat source is theoretically considered to be unnecessary to satisfy the isentropic condition. However, the result of simulation without the heat source showed a decrease of entropy across the compressor, which is considered to be unphysical. Thus we introduced the heat source as a countermeasure.

The main difference of the source terms model from the fan interface model is the progressive increase of pressure in contrary to the jump, as compared in Fig. 4(c) and (d). This has two advantages; first, the computations were numerically more stable. In the case of the fan interface model, we faced numerical instabilities when the pressure ratio of the compressor was set higher than 2.5. Here, the pressure ratio of the compressor is defined as:

$$\Pi = \frac{p_{0,a}}{p_{0,b}}, \tag{5}$$

where $p_{0,a}$ is the total pressure downstream of the fan/source region and $p_{0,b}$ is the total pressure immediately upstream of the fan/source region. The second advantage is that the progressive pressure increase approximates the phenomena in a multistage compressor more appropriately.

3.6. Power consumption

In order to assess the potential benefits of a compressor, the total power consumption of the system was considered. The pod investigated in this paper is supposed to be propelled by LIM and the compressor. This section describes the procedure to calculate the power required for both thrust systems, the LIM and the compressor, based on the CFD simulation results.

The power required by a compressor can be computed as:

$$P_{compr} = \dot{m} c_p \Delta T_0, \tag{6}$$

where $\dot{m}$ is the mass flow through the compressor, c_p is the specific heat capacity at constant pressure ($1004 \frac{J}{kg \cdot K}$ for air) and ΔT_0 is the change of total temperature across the compressor (Schobeiri, 2012). The power required by the LIM to propel the pod at a speed u is:

$$P_{LIM} = T_{LIM} \cdot u, \tag{7}$$

where T_{LIM} is the necessary thrust force, which at steady state can be computed as:

$$T_{LIM} = D_{tot} - T_{compr}, \tag{8}$$

where D_{tot} is the total drag predicted by CFD simulation and T_{compr} is the thrust provided by the compressor which is defined for each compressor model. For the fan interface model:

$$T_{compr,f} = A_{fan} \cdot \Delta p, \tag{9}$$

where Δp is the pressure difference across the fan interface and A_{fan} is the frontal area of the fan. For the source terms model, the force can be directly computed from the momentum source S_m:

$$T_{compr,s} = S_m \cdot V_s, \tag{10}$$

with V_s as the source volume, depicted in Fig. 4(b). For two simulations (one with the fan interface model, and the other with the source terms model) with the same compressor pressure ratio achieved, the compressor thrust computed with Eqs. (9) and (10) gave very similar results, the difference being around 1%.

The total power consumption is simply defined as:

$$P_{tot} = P_{LIM} + P_{compr}. \tag{11}$$

The power consumption is analyzed also by means of the non-dimensional power coefficient c_{power} which is defined as:

$$c_{power} = \frac{P_{tot}}{\frac{1}{2}\rho u^3 A_f}, \tag{12}$$

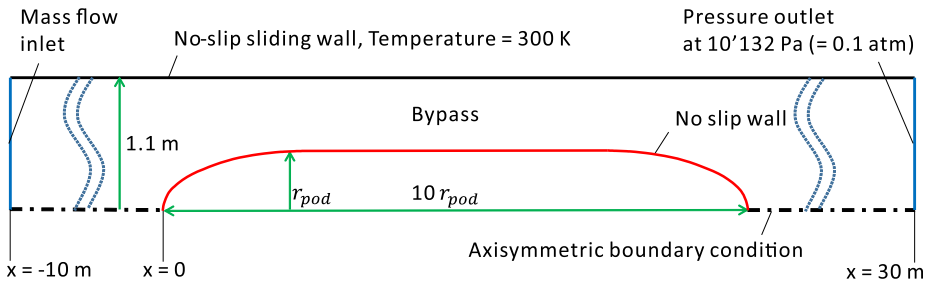

Fig. 3. Computational domain and boundary conditions.

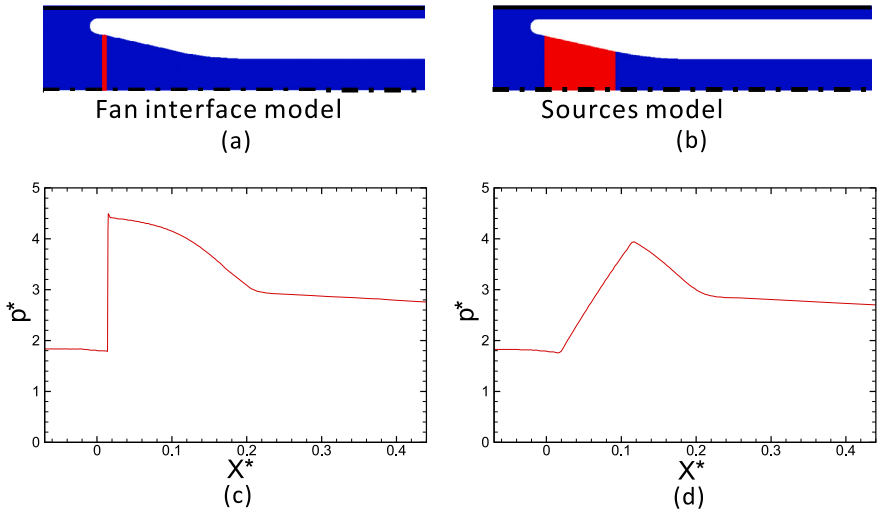

Fig. 4. Body force distribution indicated by red patch for (a) the fan interface model and (b) the source terms model. Example of pressure evolution along the axis for (c) the fan interface model and (d) the source terms model.

where ρ is the air density in the tube, u is the pod speed and A_f is the pod frontal area.

In order to assess the performance of the compressor, the following procedure was performed for each test case with different combinations of BR and pod Mach number:

- Perform a simulation deactivating the compressor,
- Activate the compressor and gradually increase the pressure ratio,
- Analyze how P_{tot} changes for different pressure ratios and find minimum P_{tot}.

4. Verification and validation

4.1. Mesh dependency study

A mesh dependency study was performed for the pod without the compressor. Four cases of simulation with different base cell sizes were computed for the pod with $BR = 0.2$ and $Ma = 0.4$. The mesh size parameters for the Prism Layer function were kept constant (as mentioned in Section 3.4). The total drag was evaluated as the function of the mesh size since it is the main interest of this study. Note that a global or local value can be selected as the evaluation function, but the global one was selected in this study based on the discussion in Roache (1997); for error estimation of useful scientific or engineering measures, local estimates are suspect, and their validity as surrogate estimators for measures of interest must be established anew for each family of nearby problems. The results are summarized in Table 1 and Fig. 5(a). Although the monotonic convergence was not achieved for the total drag, the difference becomes below 1% for base cell sizes smaller than 25 mm. Thus the base cell size of 25 mm, as shown in Fig. 5(b), is used in the following simulations in this paper.

Table 1
Mesh parameters and the computed total drag for the mesh dependency study.

Base cell size [mm]	Number of cells	Total drag [N]	Difference [%]
50	18'856	162.7	+14.1
25	71'146	142.6	–
12.5	275'932	141.3	−0.9
6.25	1'086'549	142.1	−0.4

To evaluate the mesh size on the walls, the distribution of y^+ for the base cell size of 25 mm is shown in Fig. 6. The maximum y^+ is of the order of unity for $BR = 0.2$ and $Ma = 0.4$. Of course, the computed of y^+ depends on the condition of simulation, and the value increases with the increase of BR and Ma. In the cases of maximum BR and Ma investigated in this study, i.e. $BR = 0.9$ and $Ma = 0.8$, the maximum y^+ is of the order of 10. Since the wall function used in the simulation can handle y^+ less than about 300 (Siemens PLM. Software, 2020), the mesh size on the walls is considered to be small enough.

4.2. Length of downstream region

As described in 3.3 and shown in 3, the dimension of the computational domain is set to be constant and independent from the pod length. This means that the length of downstream region becomes shorter in case that the pod length is longer. The minimum downstream length is two times of the pod length ($2L_{pod}$) for the case $BR = 0.9$, which might be too short to avoid the influence of the outlet boundary ideally. However, especially in case of the supersonic flow, the pressure waves cannot propagates towards upstream because the flow velocity in the downstream direction is faster than the pressure propagation speed towards upstream. Consequently, the region influenced by the outlet

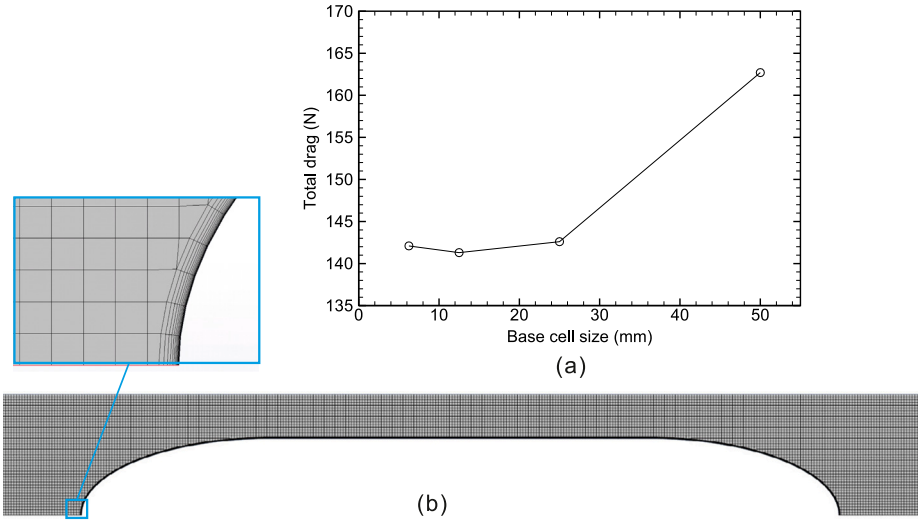

Fig. 5. (a) Computed total drag as the function of cell size and (b) the mesh for the pod without compressor with the base cell size at 25 mm.

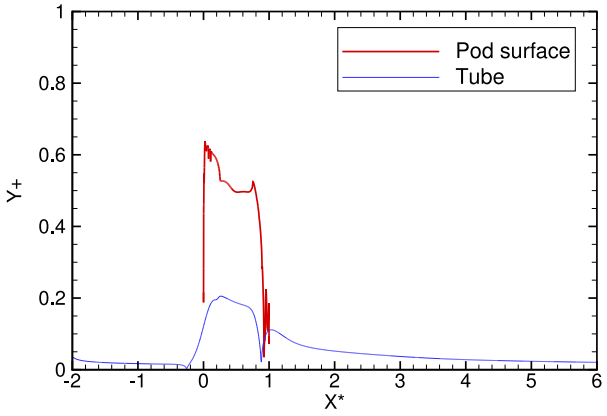

Fig. 6. Distribution of y^+ on the pod and the tube for the case $BR = 0.2$ and $Ma = 0.4$.

boundary condition is limited to proximity of the outlet as is shown in Fig. 7 for the case $BR = 0.9$ and $Ma = 0.9$.

4.3. Validation against wind tunnel measurements

As a validation case, the CFD result for the supersonic flow around a cylindrical body with hemispherical nose was compared with the wind tunnel experiment carried out by Stine and Wanlass (1955). The pod Mach number was set to 1.97 and the tunnel pressure was 2 atm. The computational domain and the boundary conditions are shown in Fig. 8. A total of 960'000 cells were used with the base size of 0.625 mm and 20 prism layers to obtain $y^+ \approx 1$. Three types of turbulence models were evaluated: the Spalart–Allmaras model, the realizable $k-\varepsilon$ model and the SST $k-\omega$ model with the two-layer all y+ wall treatment (Siemens PLM. Software, 2020). Fig. 9(a) shows the computed Mach number distribution around the body for the case using the realizable $k-\varepsilon$ model. The typical bow shock structure is observed upstream of the body, with oblique shocks around it and flow separation in the wake region. Fig. 9(b) shows the comparison of the pressure coefficient on the model surface. The dimensionless quantity s/D is computed as the ratio of the distance along the surface of the body s to the diameter of the hemispherical nose D, as indicated in Fig. 8. The pressure coefficient is defined as:

$$c_{pr} = \frac{p - p_{inf}}{\frac{1}{2}\rho_{inf} u_{inf}^2}, \tag{13}$$

where p is the static pressure, and p_{inf}, ρ_{inf} and u_{inf} are the static pressure, density and velocity in the freestream, respectively. The results of the simulation are in good agreement with the experiment (Stine and Wanlass, 1955) overall. In the fore part of the body, the realizable $k-\varepsilon$ model predicts the pressure coefficient better then the Spalart–Allmaras and SST $k-\omega$ models. The value of c_{pr} at the forefront for the realizable $k-\varepsilon$ model is 4.2% lower than the experiment (1.59 compared to 1.66), whereas for the other two models underestimate approximately 8% ($c_{pr} = 1.53$). Both the Spalart–Allmaras and the SST $k-\omega$ models predict early separation of the flow towards the rear part of the body, as illustrated in Fig. 9 (b). Based on these results, the realizable $k-\varepsilon$ model was selected for further analyzes in this paper.

4.4. Comparison of supersonic flow around the pod between CFD and 1D analytical solution

In a similar way to the analysis of the de Laval nozzle, it is possible to compute the pressure and the velocity analytically using the one-dimensional theory based on isentropic conditions. By knowing that choked flow is present in the narrowest flow-path section, the bypass, the evolution of Mach number and pressure along the pod can be analytically calculated. The flow velocity in the upstream of the pod is assumed to be the one calculated from Eq. (1) for given BR, which is slower than the pod traveling speed, in order to take into account the influence of accumulated air in front of the pod. Using this velocity, the pressure in the upstream is obtained. Based on the distribution of the pressure field, the pressure drag is calculated by integrating the product of local pressure and the axial component of the normal vector of the pod surface. The pod was without compressor, and the condition was $BR = 0.7$ at $Ma = 0.8$.

Fig. 10 shows the comparison of the pressure distribution on the pod between 1D analysis and 2D axisymmetric CFD, where $Y^* = Y$ (m) / Pod length (m). It is observed that the result of the 1D analysis shows good agreement with the CFD result, especially around the nose and the tail of the pod where the sectional area changes. The main discrepancy is observed in the constant cross-section part (from $X^* = 0.25$ to $X^* = 0.75$), since the viscous effects and consequent pressure loss are neglected in the 1D analysis. Another difference is seen around the end of the tail ($X^* = 0.95$), where the CFD result shows the flow separation in the wake. Note that the Mach number distribution shows the subsonic flow in the wake, and the pressure recovers in this region.

The pressure drag computed with the 1D analysis, 112.7 kN, is very close to the CFD result, 112.0 kN. The similarity of pressure drag between the 1D analytical solution and the axis-symmetric two-dimensional CFD simulation indicates the effectiveness of the analytical solution on the pressure drag for given simple geometry.

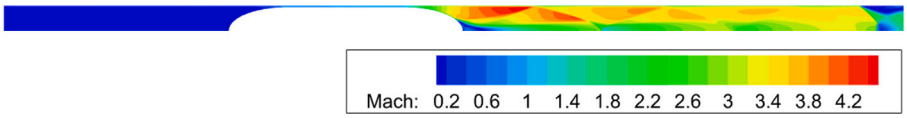

Fig. 7. Distribution of Mach number for the case $BR = 0.9$ and $Ma = 0.9$. Only the proximity of the outlet is influenced by the outlet boundary condition.

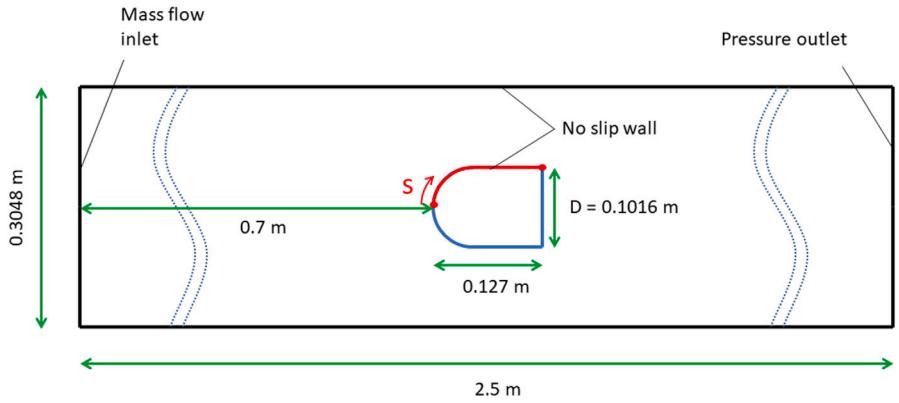

Fig. 8. Computational domain and boundary conditions for the wind tunnel validation test case (Stine and Wanlass, 1955).

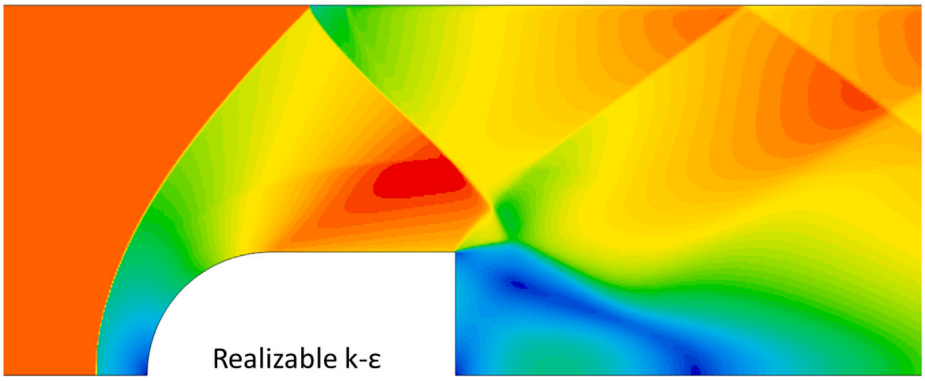

(a)

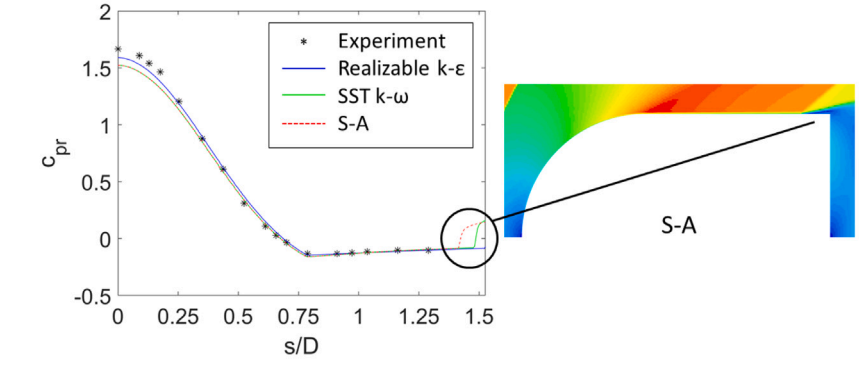

(b)

Fig. 9. (a) Computed Mach number distribution around the body with the realizable $k-\varepsilon$ model; (b)-left comparison of pressure coefficient on the body between the experiment (Stine and Wanlass, 1955) and CFD simulations with different turbulence models; (b)-right Mach number distribution for the Spalart–Allmaras (S-A) model.

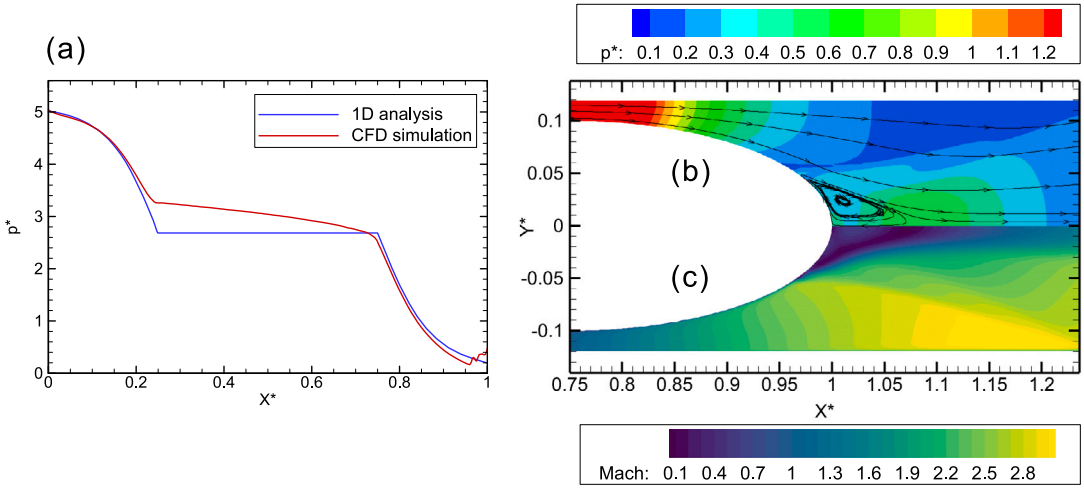

Fig. 10. (a) Comparison of pressure on the pod surface for the case $BR = 0.7$ and $Ma = 0.8$ between 1D analytical solution and 2D axisymmetric CFD simulation; (b) pressure distribution and streamlines and (c) Mach number distribution around the rear part of the pod.

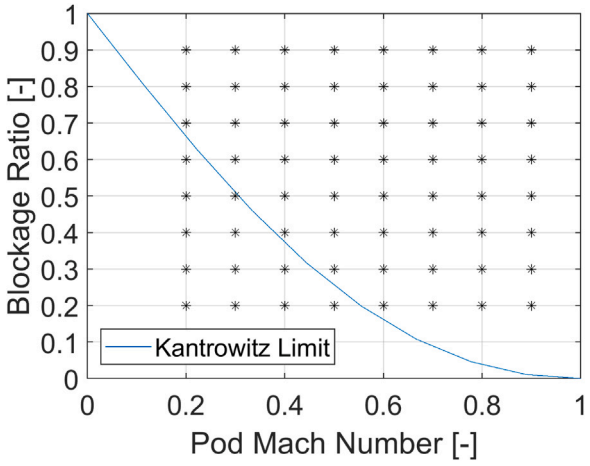

Fig. 11. Simulation cases (indicated by *) for the pod without compressor.

5. Results of CFD simulations

5.1. Pod without compressor

This section describes the results of the pod without a compressor. The flow structure and the drag were investigated. A total of 64 conditions in the parameter space of BR and Ma, depicted in Fig. 11, were simulated. The pod Mach number ranges from 0.2 to 0.9, and so does the blockage ratio, which covers both conditions below and above the KL. The Reynolds number is defined as $Re = \frac{\rho u L}{\mu}$, where ρ is the density of the air, u is the pod speed, L is the radius of the tube and μ is the dynamic viscosity of air. For the investigated conditions, Re ranges from 5.20×10^5 ($Ma = 0.2$) to 2.34×10^6 ($Ma = 0.9$).

5.1.1. Flow structure

The evolution of the flow path around a Hyperloop pod resembles the one in a de Laval nozzle; the flow sectional area once decreases, reaches the minimum and then increases again. The characteristics of the flow in the downstream of the throat (the position of minimum flow section) is determined by the geometry and the pressures upstream and downstream of the throat. For a given nozzle geometry, the pressure difference (or pressure ratio) between inlet and outlet of the nozzle determines the formation of shocks, either in the diverging part of the nozzle or at the outlet (Schobeiri, 2012). When a pod advances in the tube above the KL, the air accumulates in front and the pressure upstream increases. The amount of accumulated air, and thus the pressure, depend on the pod condition in the parameter space (BR and Ma); a faster and/or bigger pod experiences a higher pressure upstream, which changes the effective pressure ratio. Therefore, different flow structures are expected to form for different pod conditions. The simulation results confirm this hypothesis. To illustrate it, we compute three cases of simulation with different pod speeds: $Ma = 0.4$, 0.6 and 0.8. The blockage ratio is set to 0.2 for all the cases, the simulation points being plotted on the $BR - Ma$ map in Fig. 12(a). Note that for this example only the pod Mach number is increased, but the same analysis could be performed by keeping Ma constant and increasing the blockage ratio.

The pressure upstream of the pod is different between the three cases, as shown in Fig. 12(b). For the subsonic case (Case 1) the value is close to the tube pressure (10'132 Pa), while for the other two cases it is higher; $p^* = 1.13$ for Case 2 and $p^* = 1.52$ for Case 3. The distribution of Mach number is compared in Fig. 12(c). In Case 1, the flow does not choke in the bypass and stays subsonic. In Case 2, the flow chokes in the bypass, a normal shock appears around the region where the body begins to narrow. In Case 3, the pressure accumulated upstream of the pod becomes high enough to keep the flow downstream of the pod supersonic with expansion shock wave. These three cases are the representatives of the parameter space examined in this study, meaning that all the tested conditions resulted in one of those structures.

5.1.2. Drag

The total drag coefficient is defined as:

$$c_d = \frac{D_{tot}}{\frac{1}{2}\rho u^2 A_f}, \tag{14}$$

where D_{tot} is the total drag, ρ is the air density in the tube, u is the pod speed and A_f is the pod frontal area. It is worth noting that $c_d = c_{power}$ (defined in Eq. (12)) for the pod without compressor.

The predicted coefficients of the total drag c_d for all the simulated cases are shown in Fig. 13(b) and Table 2. It is clear that higher drag was computed for the region above KL. The ratio of the pressure drag to the total drag is also shown in Table 2. In the region above the KL, most of the contribution comes from the pressure drag (up to 99% of total drag) and the contribution of the friction drag is minor. For the purposes of easy understanding, the total drag and the total drag coefficient for a specific BR are shown in Fig. 14. The steep increase of the drag coefficient around $Ma = 0.4$ is caused by the KL, and the normal shock wave changes to the expansion shock wave around $Ma =$

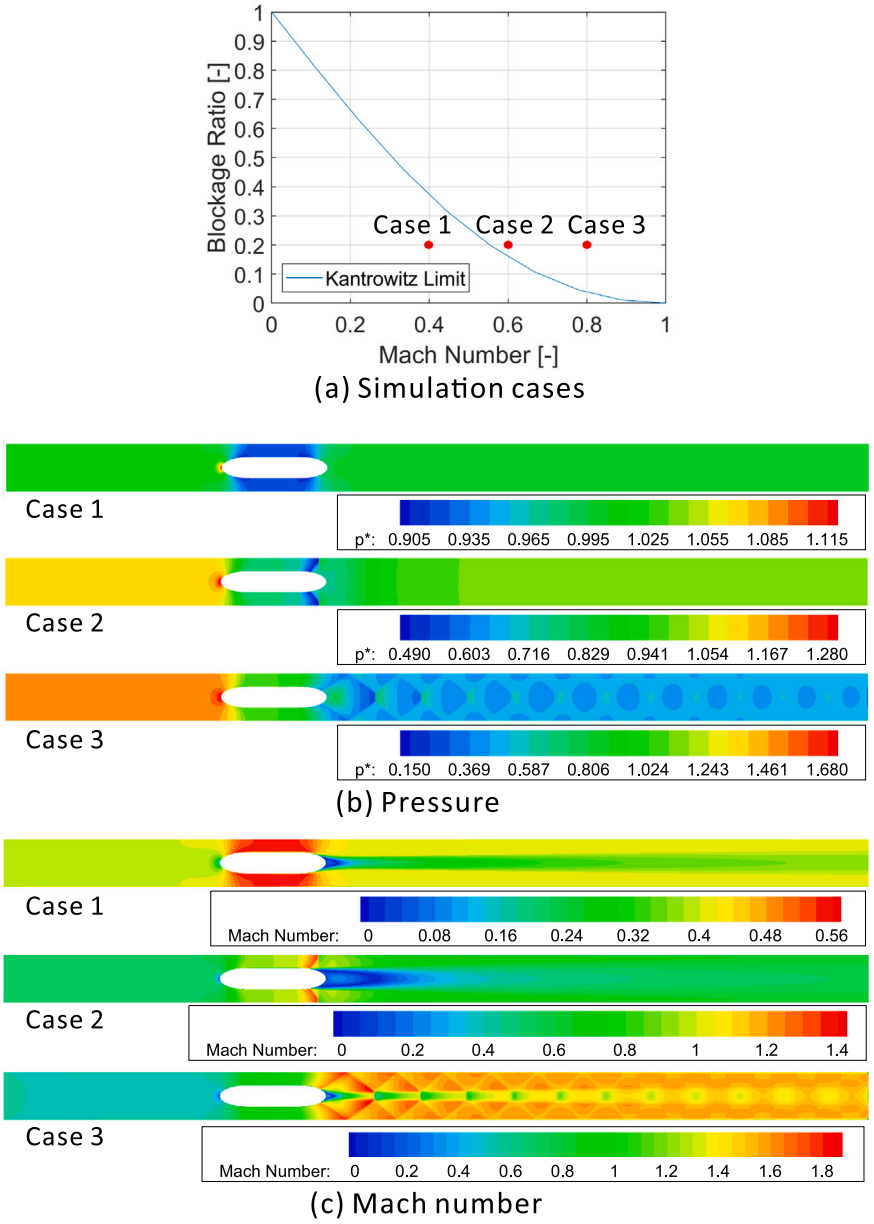

Fig. 12. (a) Simulation cases and comparison of (b) pressure distribution and (c) Mach number distribution. The flow structure for Case 1 subsonic, Case 2 supersonic with normal shock wave and Case 3 supersonic with expansion shock wave.

0.6, where the drag coefficient reaches the peak. The drag coefficient shown in Fig. 14(b) is consistent with the results published by other research groups in Kang et al. (2017) and Le et al. (2020).

5.1.3. Comparison between 2D-axisymmetric and 3D models

In order to evaluate the applicability of 2D-axisymmetric simulation results to more realistic 3D models, a 3D test case was computed for the half-model as shown in Fig. 15(a). Similarly to the design of the actual tube built for the Hyperloop competition (Space Exploration Technologies Corp., 2016), the tube was designed with a flat floor on the bottom. It should be pointed out that detailed parts of the pod, e.g. main and stability wheels and other pod peripherals, were neglected in the 3D model. The pod also has a flat part at the bottom and was positioned 0.1 m above the tube. The domain size and mesh parameters are set to the same value as the 2D cases. The mesh was coarsened twice in both upstream and downstream direction and accounts for a total number of cells being 986'415. Only one representative case was simulated: $BR = 0.7$ and $Ma = 0.8$. It is worth mentioning that the cross-sectional area of the tube in the 3D model is smaller than that in the 2D-axisymmetric model, due to the flat bottom. Thus, in order to keep the same blockage ratio, the frontal area of the pod A_f for the 3D model was also scaled to be proportionate with the 2D-axisymmetric case (as reported in Table 3).

Fig. 15(b) shows the comparison of the Mach number distribution between the 2D-axisymmetric and the 3D cases. In general, these results exhibit similar features, e.g. flow with expansion wave in the downstream of the pod. The main difference is the loss of axial symmetry that results in a slightly distinct shock pattern downstream of the pod. Table 3 compares the relevant quantities; the frontal area A_f, the total surface area A_t, the maximum Mach number, the pressure in the upstream of the pod, the total and pressure drag (D_{tot} and D_p) and the corresponding drag coefficients (c_d and $c_{d,p}$). The total drag coefficient is defined in Eq. (14), and the pressure drag coefficient is defined as:

$$c_{d,p} = \frac{D_p}{\frac{1}{2}\rho u^2 A_f}, \tag{15}$$

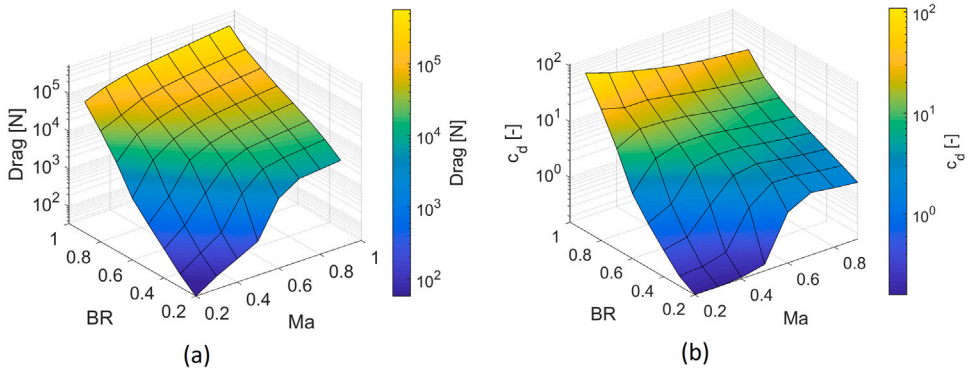

Fig. 13. (a) Drag and (b) drag coefficient at different BR and Ma for the pod without compressor.

Table 2
Computed total drag coefficient and the ratio of pressure drag to total drag in brackets [%].

		Ma							
		0.2	0.3	0.4	0.5	0.6	0.7	0.8	0.9
BR	0.9	108.90 (98.9)	78.99 (99.0)	61.46 (99.0)	49.18 (99.1)	40.60 (99.1)	35.15 (99.1)	31.70 (99.1)	28.72 (99.1)
	0.8	35.63 (98.1)	27.25 (98.5)	27.12 (98.7)	23.02 (98.8)	19.43 (98.8)	16.79 (98.8)	14.71 (98.8)	13.30 (98.8)
	0.7	10.21 (95.3)	16.66 (98.0)	15.98 (98.4)	14.50 (98.6)	12.24 (98.6)	10.56 (98.6)	9.25 (98.7)	8.34 (98.7)
	0.6	2.32 (87.7)	7.11 (96.6)	9.42 (97.9)	9.38 (98.3)	8.29 (98.4)	7.16 (98.4)	6.28 (98.4)	5.66 (98.5)
	0.5	0.99 (80.4)	1.57 (87.8)	5.30 (97.8)	6.33 (98.1)	6.07 (98.1)	5.25 (98.1)	4.60 (98.1)	4.15 (98.2)
	0.4	0.47 (70.3)	0.58 (76.8)	1.57 (91.3)	3.87 (96.9)	4.51 (97.6)	3.89 (97.7)	3.41 (97.7)	3.08 (97.8)
	0.3	0.24 (55.0)	0.25 (60.0)	0.33 (69.8)	1.50 (93.6)	3.01 (97.0)	2.88 (97.3)	2.52 (97.3)	2.27 (97.4)
	0.2	0.16 (43.1)	0.16 (46.0)	0.17 (51.3)	0.21 (61.1)	1.29 (93.7)	2.09 (96.3)	1.83 (96.4)	1.65 (96.5)

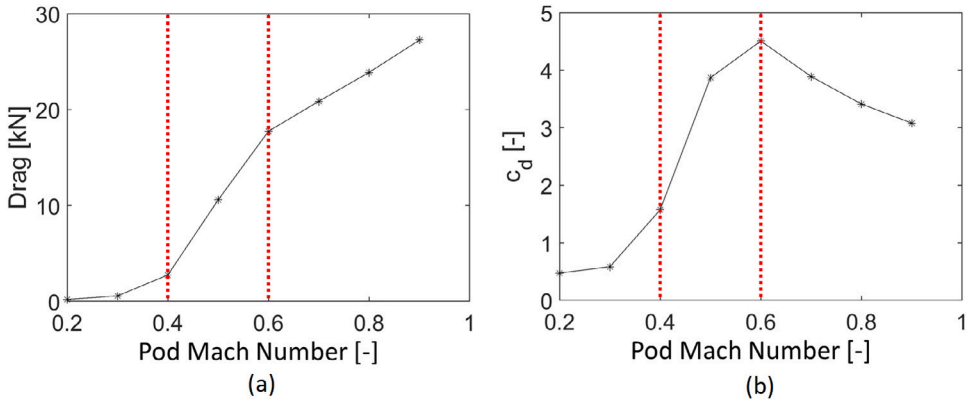

Fig. 14. (a) Drag and (b) drag coefficient for the pod without compressor with $BR = 0.4$ at different pod Mach number.

where D_p is the pressure drag.

The total drag and pressure drag for the 3D case are 6.6% and 10.4% smaller than those for the 2D-axisymmetric case, respectively. This is considered to be caused by the smaller frontal area A_f, since the difference of c_d and $c_{d,p}$ is relatively small, i.e. 2.8% and −1.9%, respectively. In fact, the predicted accumulated pressure in front is similar between the two cases. In this light, we adopt the 2D-axisymmetric configuration for the rest of the study.

5.2. Pod with compressor

The previous section aimed to show the increase in the drag above the KL quantitatively. For the cases further above the KL (high BR and Ma), the high pressure accumulated in front of the pod can increase up to more than 60'000 Pa (∼ six times higher than the tube system pressure), which partially causes the increase of the drag of three orders of magnitude. This motivates us to investigate the potential benefit of implementing an axial compressor. The simulated conditions of BR and Ma are shown in Fig. 16. The blockage ratio varies from 0.24 to 0.72 every 0.08, in combination with four pod Mach numbers: 0.2, 0.4, 0.6, 0.8. Each point was simulated for several compressor pressure ratios, which was progressively increased until a maximum value of approximately 3.5. This procedure was performed with both modeling approaches. Conditions below the KL were not tested since the contribution of a compressor is expected to be negligible (i.e. when the flow is not choked, no accumulation of air upstream occurs).

5.2.1. Effects of compressor

First, we evaluate both modeling approaches for the compressor, i.e. the fan interface model and the source terms model, for a sample case with $BR = 0.72$ and $Ma = 0.6$. Fig. 17 compares the distribution of Mach number and non-dimensionalized pressure $p*$ between the fan interface model and the source terms model. The pressure ratio for the compressor was set to 2.2 for the both models. The Mach number fields are very similar; a strong expansion with oblique shocks is visible at the outlet of the duct, with comparable maximum Mach numbers of 4.28 for the fan interface model and 4.42 for the source terms model. It should be pointed out that the flow stays supersonic in the downstream of the pod. The pressure fields are different due to the nature of the methods; the fan interface model sharply increases the

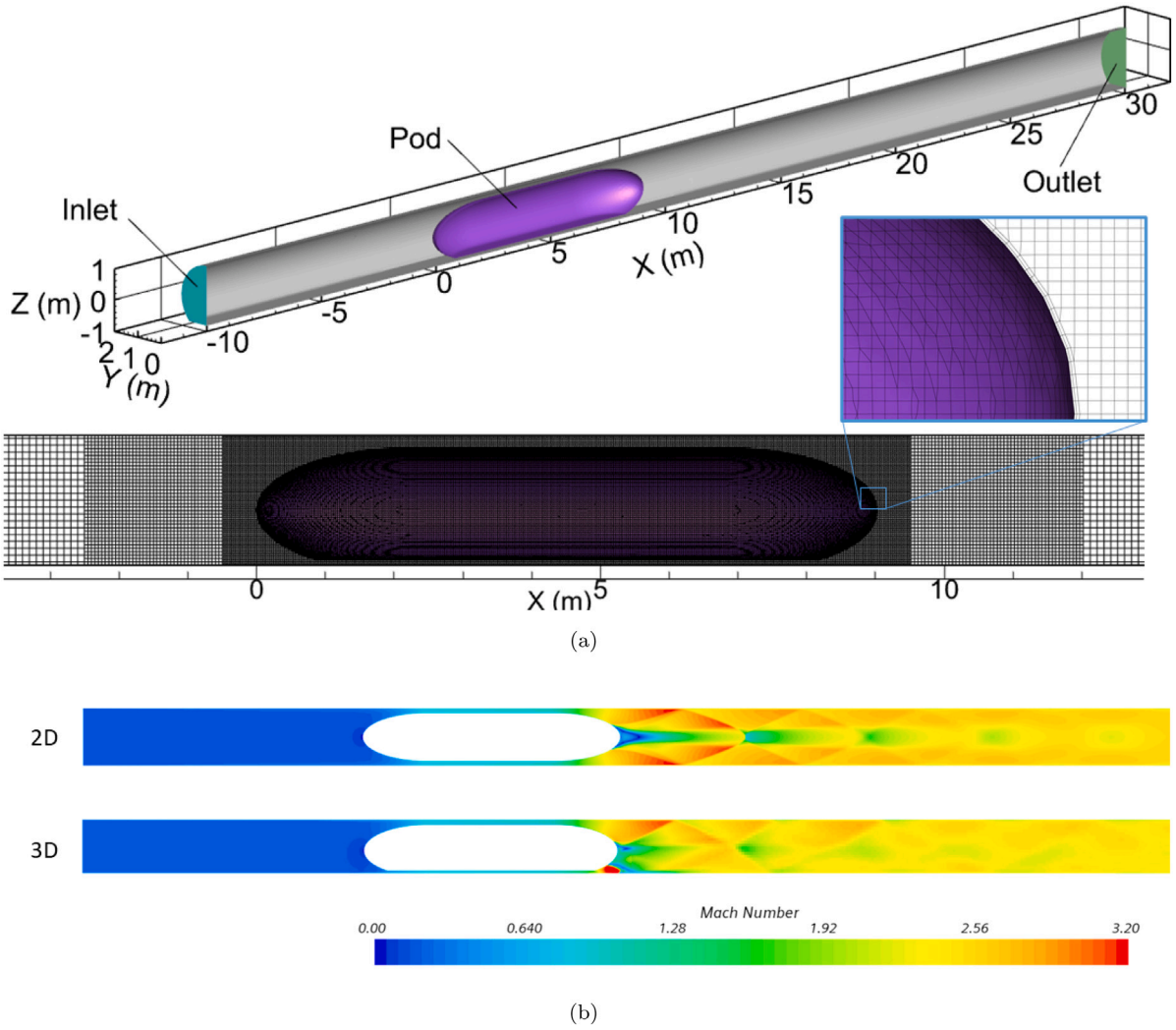

Fig. 15. (a) Computational domain and mesh for 3D simulation and (b) comparison of Mach number distribution between 2D-axisymmetric and 3D simulations. The distribution on the symmetry plane is depicted for the 3D case.

Table 3
Comparison between 2D-axisymmetric and 3D simulations.

	A_f [m^2]	A_t [m^2]	Max. Ma [–]	p in front [Pa]	D_{tot} [kN]	D_p [kN]	c_d [–]	$c_{d,p}$ [–]
2D-axisymmetric	2.66	48.95	3.18	51'000	113.0	111.5	9.25	9.13
3D	2.43	46.50	3.38	49'400	106.0	99.9	9.51	8.96
Difference [%]	−8.6	−5.0	6.2	−3.2	−6.6	−10.4	2.8	−1.9

pressure at the specified plane, while the source terms model shows progressive increase. The pressure fields shown in figures (c) and (d) differ in the initial part of the converging section, but reaches similar values in the duct, i.e. $p* = 3.0$ for both models at the end of duct.

Fig. 18(a) shows how the mass flow through the duct changes with the increase of the compressor pressure ratio for both models. Two observations can be made in this part: first, the two models achieve almost the same mass flow for the same pressure ratio. This demonstrates that the two distinct approaches achieve the same effects on the flow. Second, the mass flow increases with the increase of the compressor pressure ratio, as is expected. The same trend is observed for all the simulation cases of BR and Ma.

Fig. 18(b) shows how the accumulated pressure in front of the pod changes with the increase of the compressor pressure ratio for the same reference case with $BR = 0.72$ $Ma = 0.6$. The absolute pressure is reduced approximately from 40'000 Pa to 20'000 Pa when the compressor operates at the pressure ratio of 3.5. Similar results are again observed for both approaches. The same trend was also observed for all the other simulation cases with different BR and Ma. In Table 4 we report the effects of the compressor for other selected cases; the accumulated pressure in front when the compressor is idle, the highest compressor pressure ratio simulated, the pressure in front for that operating condition and the reduction ratio of the accumulated pressure in front.

Since it was shown that the solution computed with the two models for the compressor are very similar, we only present the results calculated with the source terms model hereafter.

5.2.2. Power consumption and optimal cases

The total power consumption of the pod with compressor is considered in order to assess the effectiveness of the compressor. The total power consumption is the sum of the power used by the LIM and by the compressor, as defined in Section 3.6. Fig. 19 shows how the normalized power consumption for the selected cases varies with

Table 4
Effects of compressor on accumulated pressure in front, selected cases.

Case	p in front, deactivating compressor [Pa]	Compressor pressure ratio [–]	p in front, activating compressor [Pa]	Reduction [%]
BR 0.56, Ma 0.4	16'450	2.9	11'200	32
BR 0.56, Ma 0.6	25'100	3.5	15'900	36.7
BR 0.56, Ma 0.8	33'750	3.9	20'650	38.8
BR 0.72, Ma 0.4	26'850	2.7	14'950	44.3
BR 0.72, Ma 0.6	40'900	3.4	20'200	50.6
BR 0.72, Ma 0.8	55'100	3.8	25'500	53.7

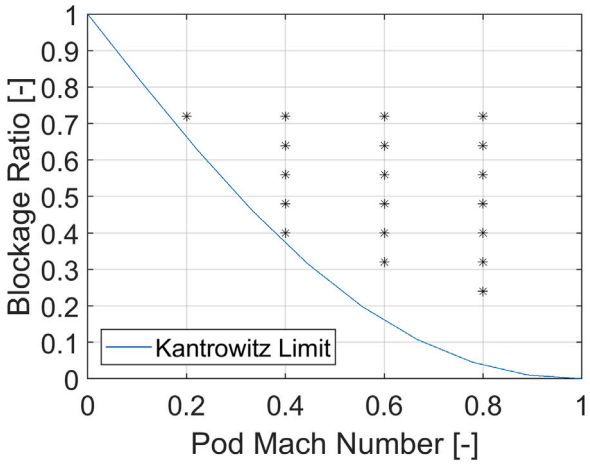

Fig. 16. Simulation cases (indicated by *) for the pod with compressor.

the compressor pressure ratio. A pressure ratio of 1 indicates that the compressor is not active. P_{tot} is normalized with the total power consumption when the compressor is not active. Thus, a normalized value below 1 for a particular compressor pressure ratio indicates that the compressor is able to reduce the total power consumption. Fig. 19(a) shows the results for $BR = 0.4$ and $Ma = 0.4$, 0.6 and 0.8, while Fig. 19(b) shows $BR = 0.72$ and the same Mach numbers.

The following observations can be made; the compressor can reduce the total power consumption for most of the cases, except one simulation case with $BR = 0.4$ and $Ma = 0.4$. The result implies that the compressor is not beneficial for the case with low BR and low Ma. For the cases whose power consumption is reduced, there could be an optimal compressor pressure ratio at which the power consumption reaches the minimum. This is clear for the case with $BR = 0.72$ and $Ma = 0.4$. For the cases with higher BR and Ma, e.g. $BR = 0.72$ and $Ma = 0.6$ or 0.8, the optimal pressure ratio could not be found in the range $\Pi < 4$. It is worth mentioning that we could not perform simulations with $\Pi > 4$ because of numerical instabilities. The minimum power consumptions for different BR and Ma within the range $1 < \Pi < 4$ are shown in Fig. 20(a) together with the applied pressure ratio Π in Fig. 20(b). The solution is linearly interpolated between the computed nodes (cases). For example, for $BR = 0.72$ and $Ma = 0.4$, a compressor operating at a pressure ratio of 2.02 could reduce the power consumption by 16.3%. The maximum gain in power usage occurs at the most extreme case, i.e. $BR = 0.72$ and $Ma = 0.8$. With a compressor pressure ratio of 3.8, 47.5% of power consumption can be saved, according to this analysis. The reduction in power consumption is in line with the results obtained by Lluesma-Rodríguez et al. (2021). The different magnitude in the power reduction is supposedly due to the different models used to emulate the compressor. While in this study, the computational domain includes the compressed-air path, the authors in Lluesma-Rodríguez et al. (2021) set boundary conditions at the head and tail of the pod. This effectively changes the computed drag on the pod and ultimately the computed power consumption, and explains the main deviation in the obtained results.

These results are also summarized in Table 5, where the horizontal dash indicates that the total power consumption was not reduced by the compressor.

The effectiveness of the compressor could be summarized as follows:

- The total power consumption can be reduced with a compressor for most of the simulated cases above the KL.
- Higher benefits are obtained for the cases with higher BR and Ma.
- The optimum compressor pressure ratio also increases with the increase of BR and Ma.

Finally, Table 6 shows a comparison of the power coefficient c_{power} between the two pod designs. The values for the pod without compressor were calculated by linearly interpolating those in Table 2 because of the different blockage ratios simulated. The benefits of a compressor are higher for conditions with higher BR and Ma, with a reduction of c_{power} of 44% for the case with $BR = 0.72$ and $Ma = 0.8$. On the other hand, the power coefficient of the pod with compressor is higher for conditions which are slightly above the KL, indicating that a compressor can only be beneficial for sufficiently higher blockage ratios and Mach numbers.

5.2.3. Influence of the tube operating pressure

The influence of the tube pressure on the compressor performance was investigated by changing the tube pressure p_{tube} from 0.1 atm to 0.01 atm. One specific blockage ratio of 0.72 and three Mach numbers 0.4, 0.6, 0.8 were simulated with the lower tube pressure. The same procedure to find the minimum power consumption taken in Section 5.2.2 was used. Fig. 21 shows the non-dimensionalized power coefficient c_{power}, defined by Eq. (12), as a function of the compressor pressure ratio for the case with $BR = 0.72$ and $Ma = 0.8$, for the different tube pressures. c_{power} is independent from p_{tube} and the compressor has the same effect on the reduction of the non-dimensionalized power consumption. The same feature was observed for the cases with $Ma = 0.4$ and 0.6. In fact this is expected since all the relevant quantities for the calculation linearly depend on the tube pressure; mass flows, drag, compressor power. Therefore, it can be concluded that the non-dimensionalized results computed are valid at least within the tube pressures 0.01–0.1 atm.

5.2.4. Influence of system scaling

The effects of changing the system size were studied by scaling both tube and pod sizes by the factor of 0.5. The configurations with $BR = 0.72$ and $Ma = 0.4$, 0.6, 0.8 were considered. The total drag coefficient (defined in Eq. (14)) for a pod Mach number of 0.8 and the original size is $c_d = 11.00$, while for the scaled model $c_d = 11.05$. The increase is expected since decreasing the system's size decreases the Reynolds number, but the difference is small because c_d is almost constant in the turbulent flow regime (Schlichting and Gersten, 2017). The Reynolds numbers for the simulated cases are listed in Table 7.

The same procedure used in Section 5.2.2 was adopted to compute the total power consumption. Fig. 22 shows the non-dimensionalized

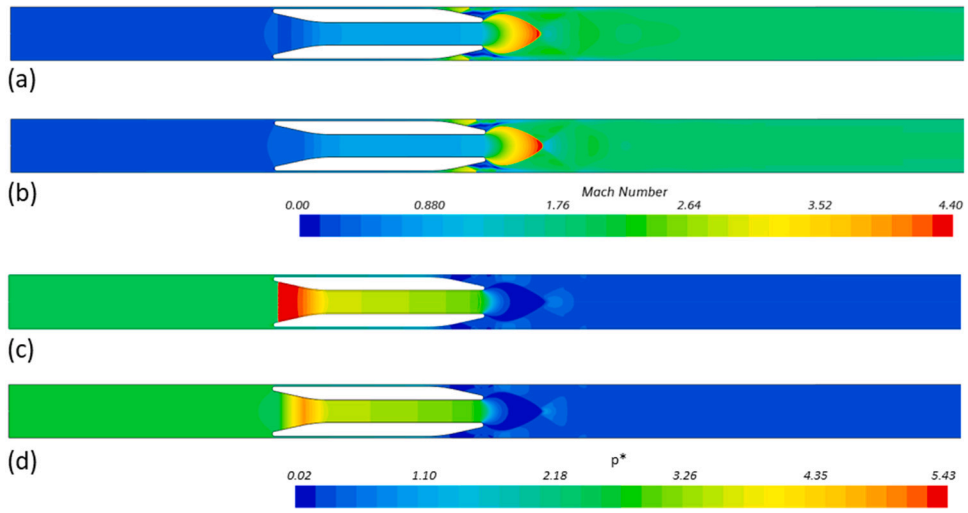

Fig. 17. Comparison between the fan interface model and the source-term model: Mach number distribution for (a) the fan interface model and (b) the source-term model, and non-dimensionalized pressure distribution for (c) fan interface and (d) source-term.

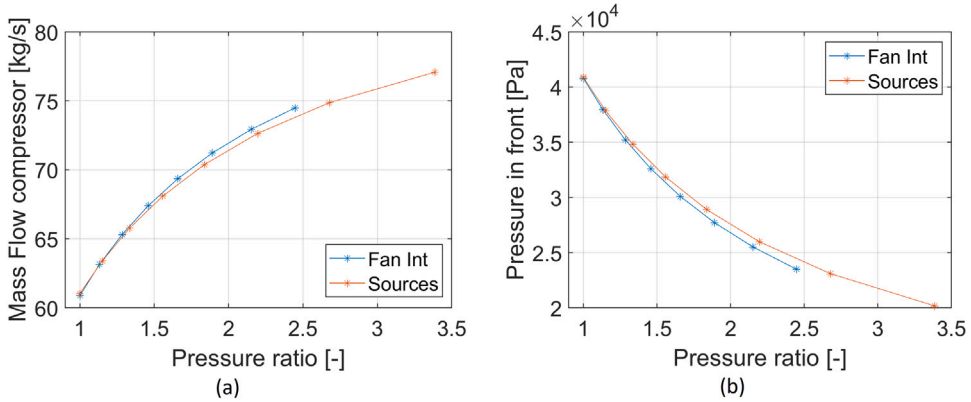

Fig. 18. Comparison of (a) mass flow through the compressor and (b) pressure in front of the pod, between the fan interface model (Fan Int) and the source terms model (Sources) for the case $BR = 0.72$ and $Ma = 0.6$.

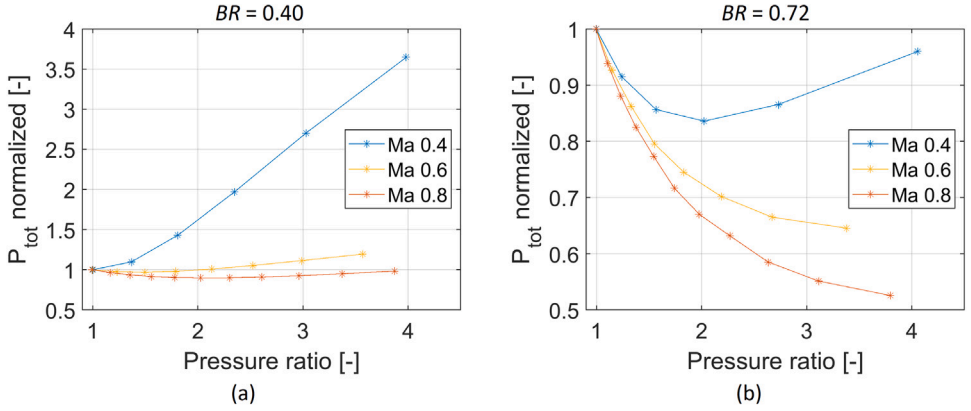

Fig. 19. Normalized total power consumption as the function of the compressor pressure ratio for different pod Mach number; (a) $BR = 0.4$ and (b) $BR = 0.72$.

power coefficient as a function of the compressor pressure ratio for the case with $BR = 0.72$ and $Ma = 0.8$, for the original and the scaled setups. The same effects of the compressor on the non-dimensionalized power consumption are observed, as expected. Therefore, the results of the performed analysis are considered to be valid for different system sizes, as long as the scaling factor is within a reasonable range, i.e. the flow regime remains turbulent.

6. Conclusions

In this paper, we investigated the aerodynamic performance of a Hyperloop pod equipped with an axial compressor using CFD simulation. The axial compressor is expected to reduce the drag especially when the pod exceeds the Kantrowitz Limit (KL). In order to evaluate the effectiveness of the compressor, two types of pod were designed:

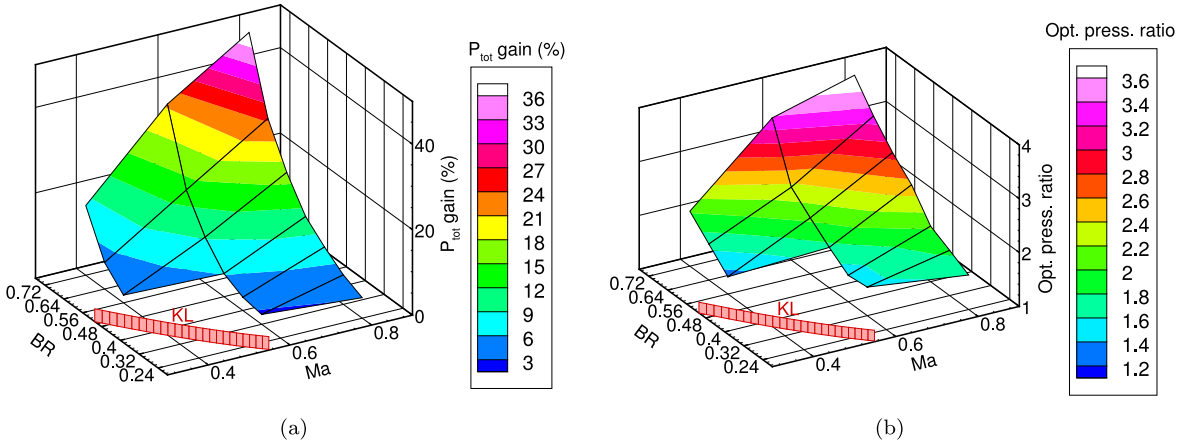

Fig. 20. (a) Optimal gains in total power consumptions and (b) corresponding compressor pressure ratio.

Table 5
Results for the tested cases at optimal pressure ratio.

Case	P_{tot} no compr. [MW]	Optimal p-ratio [–]	P_{compr} at optimal [MW]	P_{tot} at optimal [MW]	c_{power} at optimal [–]	Power gain [%]
BR 0.24, Ma 0.8	3.10	1.64	0.71	2.95	2.54	4.8
BR 0.32, Ma 0.6	2.62	1.53	0.63	2.56	3.91	2.3
BR 0.32, Ma 0.8	4.95	1.84	1.42	4.61	2.97	6.9
BR 0.40, Ma 0.4	5.95	–	–	–	–	–
BR 0.40, Ma 0.6	4.21	1.49	0.83	4.08	5.00	3.1
BR 0.40, Ma 0.8	7.56	2.03	2.45	6.79	3.51	10.2
BR 0.48, Ma 0.4	1.46	–	–	–	–	–
BR 0.48, Ma 0.6	6.11	1.75	1.69	5.78	5.90	5.4
BR 0.48, Ma 0.8	10.95	2.54	4.76	9.41	4.05	14.1
BR 0.56, Ma 0.4	2.86	1.32	0.63	2.81	8.29	1.8
BR 0.56, Ma 0.6	9.18	2.04	3.12	8.20	7.17	10.7
BR 0.56, Ma 0.8	16.43	2.88	7.41	12.95	4.77	21.2
BR 0.64, Ma 0.4	4.81	1.67	1.72	4.51	11.65	6.2
BR 0.64, Ma 0.6	13.61	2.35	5.11	11.09	8.49	18.5
BR 0.64, Ma 0.8	24.41	3.30	10.81	16.96	5.47	30.6
BR 0.72, Ma 0.2	8.67	–	–	–	–	–
BR 0.72, Ma 0.4	8.09	2.02	3.41	6.77	15.54	16.3
BR 0.72, Ma 0.6	21.42	3.38	10.02	13.83	9.41	35.4
BR 0.72, Ma 0.8	38.52	3.8	15.30	20.24	5.81	47.5

Table 6
Comparison of the power consumption coefficient c_{power} between the pods without (wo) and with compressor, the design being depicted in Fig. 2 (a) and (b) respectively. The region shaded in green represents the condition in which lower power consumption is achieved owing to the compressor. The operating compressor pressure ratio is indicated in Table 5.

BR		Ma = 0.4	Ma = 0.6	Ma = 0.8
0.72	wo comp.	18.21	13.68	10.34
	with comp. (vs wo comp. %)	15.54 (–15%)	9.41 (–31%)	5.81 (–44%)
0.64	wo comp.	12.04	9.87	7.47
	with comp. (vs wo comp. %)	11.65 (–3%)	8.49 (–14%)	5.47 (–27%)
0.56	wo comp.	7.77	7.40	5.61
	with comp. (vs wo comp. %)	8.29 (7%)	7.17 (–3%)	4.77 (–15%)
0.48	wo comp.		5.76	4.36
	with comp. (vs wo comp. %)		5.90 (2%)	4.05 (–7%)
0.40	wo comp.		4.51	3.41
	with comp. (vs wo comp. %)		5.00 (11%)	3.51 3%)
0.32	wo comp.		3.35	2.66
	with comp. (vs wo comp. %)		3.91 (17%)	2.97 (12%)
0.24	wo comp.			2.11
	with comp. (vs wo comp. %)			2.54 (21%)

Table 7
Reynolds numbers for original and half-size model at different pod Mach numbers.

	Ma = 0.4	Ma = 0.6	Ma = 0.8
Original	1.04×10^6	1.56×10^6	2.08×10^6
Half size	5.02×10^5	7.80×10^5	1.04×10^6

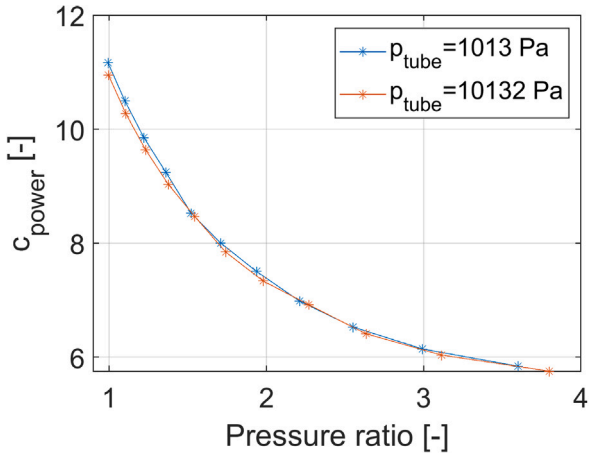

Fig. 21. Comparison of the power coefficient c_{power} between different tube pressures for the case $BR = 0.72$ and $Ma = 0.8$.

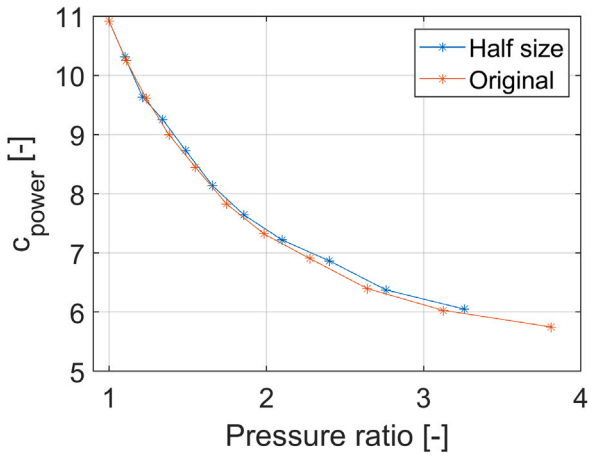

Fig. 22. Comparison of the power coefficient c_{power} between the original and half model for the pod $BR = 0.72$ and $Ma = 0.8$.

pods with and without a compressor. The pod with a compressor has a duct at the center of the body, through which the compressed air passes. The main design variables were the blockage ratios, whereas other particulars such as tube diameter, the ratio of pod length to the pod diameter and the ratio of duct diameter to pod diameter were kept constant.

In our simulations, the compressible Navier–Stokes equations were solved by using the commercial CFD code STAR-CCM+. As a validation case, we computed the flow around a cylindrical body in the supersonic regime, and the results were compared against the wind tunnel experiment done by NASA (Stine and Wanlass, 1955). The computed pressure on the body showed good agreement with the measurement, the realizable $k-\varepsilon$ turbulence model being better than the SST $k-\omega$ and the Spalart–Allmaras models. In addition to this validation, we further compared the pressure drag of a pod without compressor between the 2D-axisymmetric CFD simulation and 1D theoretical analysis based on isentropic condition in supersonic regime. Despite the simplicity of the 1D theoretical analysis which depends only on the change of the flow sectional area the predicted pressure drag matched the analytical solution very well, the difference being less than 1%. To assess the applicability of 2D-axisymmetric CFD simulations to a more realistic three-dimensional flow configuration, a 3D CFD simulation was performed for the pod without compressor, and the velocity field and the total drag were compared with those calculated with a 2D axisymmetric simulation. The difference of total drag was 6.6%, which is considered to be caused by the flat bottom shape of the pod and the tube in the 3D simulation. A mesh dependency study was performed for a pod without a compressor. It was found that a base cell size of 25 mm for the bulk region and 20 layers of thin cells with a minimum thickness of 0.025 mm for the region near the wall were fine enough to predict the grid-independent total drag. Based on these results, we used 2D-axisymmetric CFD simulations with the realizable $k-\varepsilon$ turbulence model employing the aforementioned mesh configuration.

The simulation results for the pod without compressor with different BR and pod speed showed three distinct flow regimes: subsonic flow, supersonic flow with a normal shock, and supersonic flow with oblique shocks, which are consistent with the theory of the de Laval nozzle. The drag coefficient reached the maximum value at the KL, and it decreased with an increase of Mach number above KL.

The axial compressor was modeled by two different approaches: the fan interface model implemented in the STAR-CCM+ code and the source terms model developed as a user-defined function. The source terms model was developed because the fan interface model introduced numerical instabilities when the pressure ratio of the compressor was set higher than 2.5 in our simulations. The results of both models were qualitatively and quantitatively very similar; the mass flow through the compressor progressively increased by increasing the pressure ratio of the compressor, while the accumulated pressure in front of the pod decreases, which are considered to be reasonable qualitatively.

In order to assess the benefits of a compressor, a power consumption analysis was conducted. The total power consumption of pods traveling above the KL was almost always reduced by using the compressor compared to when the compressor was at idle. The gain in power consumption increased for the cases with higher pod speed; the maximum gain was 47.5%. The pressure ratio at which the compressor should operate also increases with the excess of KL.

Ultimately, the power consumption between the two pod designs, without and with compressor, was compared. The pod with compressor operating at the optimal pressure ratio used less power for several simulation cases, with gains up to 44% for the condition $BR = 0.72$ and $Ma = 0.8$. On the other hand, the power consumption of the pod with compressor is higher for conditions slightly above the KL, indicating that the compressor is only beneficial for sufficiently higher blockage ratios and Mach numbers.

To evaluate the generality of CFD simulation results with respect to the model scale and the system pressure, simulations with half a scale and one tenth of the system pressure were performed. The results showed that the non-dimensional numbers such as the drag coefficient and the normalized total power were almost independent of the scale and the system pressure. In addition, the effectiveness of the compressor was not influenced by these parameters within the investigated ranges.

The presented work is one of the first attempts to investigate the aerodynamics related to the implementation of an axial compressor to the Hyperloop pod and can lay the foundation for future studies aimed at making progress in the evacuated tube transport systems.

CRediT authorship contribution statement

Maurice Bizzozero: Writing – original draft, Conceptualization, Methodology. **Yohei Sato:** Writing – review & editing, Technical discussion, Supervision. **Mohamed Aly Sayed:** Writing – review, Technical discussion, Supervision.

Declaration of competing interest

The authors declare that they have no known competing financial interests or personal relationships that could have appeared to influence the work reported in this paper.

Acknowledgments

This work was supported by Dr. Oliver Taheny at Siemens Digital Industries Software for the usage of STAR-CCM+. The authors thank Prof. Dr. Patrick Jenny at ETH Zürich, Mr. Fabio Dubois at EuroTube Foundation, Ms. Nathalie Nick at Swissloop as well as Dr. Ioannis Mantzaras at Paul Scherrer Institute for the helpful discussions.

References

Bose, A., Viswanathan, V.K., 2021. Mitigating the piston effect in high-speed hyperloop transportation: a study on the use of aerofoils. Energies 14 (2), 464. http://dx.doi.org/10.3390/en14020464.

Braun, J., Sousa, J., Pekadan, C., 2017. Aerodynamic design and analysis of the hyperloop. In: 55th AIAA. http://dx.doi.org/10.2514/1.J055634.

Chen, G., 2005. Nanoscale Energy Transport and Conversion: A Parallel Treatment of Electrons, Molecules, Phonons, and Photons. Oxford University Press, New York.

Chen, X., Zhao, L., Ma, J., Liu, Y., 2012. Aerodynamic simulation of evacuated tube maglev trains with different streamlined designs. J. Mod. Transp. 20 (2), 115–120. http://dx.doi.org/10.1007/bf03325788.

Chin, J.C., Gray, J.S., Jones, S.M., Berton, J.J., 2015. Open-source conceptual sizing models for the hyperloop passenger pod. In: 56th AIAA/ASCE/AHS/ASC Structures, Structural Dynamics, and Materials Conference. http://dx.doi.org/10.2514/6.2015-1587.

Decker, K., Chin, J., Peng, A., Summers, C., Nguyen, G., Oberlander, A., Sakib, G., Sharifrazi, N., Heath, C., Gray, J., Falck, R., 2017. Conceptual feasibility study of the hyperloop vehicle for next-generation transport. In: AIAA SciTech Forum - 55th AIAA Aerospace Sciences Meeting, No. January. http://dx.doi.org/10.2514/6.2017-0221.

Eurostat (European Commission), 2013. Energy, Transport and Environment Indicators. p. 252. http://dx.doi.org/10.2785/4663.

EuroTube Foundation, 2019. Ouvrage Alphatube – Collombey-Muraz Rapport succinct pour information publique.

Hu, X., Deng, Z., Zhang, W., 2021. Effect of cross passage on aerodynamic characteristics of super-high-speed evacuated tube transportation. J. Wind Eng. Ind. Aerodyn. 211, http://dx.doi.org/10.1016/j.jweia.2021.104562.

Hyde, D.J., Barr, L.C., Taylor, C.L., 2016. Hyperloop Commercial Feasibility Analysis. US Department of Transportation.

Jufer, M., Perret, F.-L., Descoeudres, F., Trottet, Y., 1993. Swissmetro, an efficient intercity subway system. Struct. Eng. Int. 3 (3), 184–189. http://dx.doi.org/10.2749/101686693780607921.

Kang, H., Jin, Y., Kwon, H., Kim, K., 2017. A study on the aerodynamic drag of transonic vehicle in evacuated tube using computational fluid dynamics. Int. J. Aeronaut. Space Sci. 18 (4), 614–622. http://dx.doi.org/10.5139/IJASS.2017.18.4.614.

Kantrowitz, A., Donaldson, C., 1945. Preliminary Investigation of Supersonic Diffusers. National Aeronautics and Space Admin Langley Research Center Hampton VA.

Kim, T.K., Kim, K.H., Kwon, H.B., 2011. Aerodynamic characteristics of a tube train. J. Wind Eng. Ind. Aerodyn. 99 (12), 1187–1196. http://dx.doi.org/10.1016/j.jweia.2011.09.001.

Le, T.T.G., Jang, K.S., Lee, K.S., Ryu, J., 2020. Numerical investigation of aerodynamic drag and pressure waves in hyperloop systems. Mathematics 8 (11), http://dx.doi.org/10.3390/math8111973.

Lluesma-Rodríguez, F., González, T., Hoyas, S., 2021. CFD simulation of a hyperloop capsule inside a low-pressure environment using an aerodynamic compressor as propulsion and drag reduction method. Appl. Sci. 11 (9), 3934. http://dx.doi.org/10.3390/app11093934.

Musk, E., 2013. Hyperloop alpha. SpaceX. [Online]; https://www.spacex.com/sites/spacex/files/hyperloop_alpha-20130812.pdf. (Accessed 15 October 2020).

Nick, N., Sato, Y., 2020. Computational fluid dynamics simulation of Hyperloop pod predicting laminar–turbulent transition. Railw. Eng. Sci. 28 (1), 97–111. http://dx.doi.org/10.1007/s40534-020-00204-z.

Niu, J., Yang, Yu, Q., Cao, X., Yuan, Y., 2019. Numerical study on the impact of Mach number on the coupling effect of aerodynamic heating and aerodynamic pressure caused by a tube train. J. Wind Eng. Ind. Aerodyn. 190, 100–111. http://dx.doi.org/10.1016/j.jweia.2019.04.001.

Oh, J.S., Kang, T., Ham, S., Lee, K.S., Jang, Y.J., Ryou, H.S., Ryu, J., 2019. Numerical analysis of aerodynamic characteristics of Hyperloop system. Energies 12 (3), http://dx.doi.org/10.3390/en12030518.

Opgenoord, M.M., Caplan, P.C., 2017. On the aerodynamic design of the hyperloop concept. In: 35th AIAA Applied Aerodynamics Conference, 2017. http://dx.doi.org/10.2514/6.2017-3740.

Roache, P., 1997. Quantification of uncertainty in computational fluid dynamics. Annu. Rev. Fluid Mech. 29, 123–160.

Roe, P.L., 1986. Characteristic-based schemes for the euler equations. Annu. Rev. Fluid Mech. 18 (1), 337–365. http://dx.doi.org/10.1146/annurev.fl.18.010186.002005.

Salter, R.M., 1972. The Very High Speed Transit System. RAND Corporation, p. 20.

Schafer, A., Victor, D.G., 2000. The future mobility of the world population. Transp. Res. A 34, 171–205. http://dx.doi.org/10.1016/S0965-8564(98)00071-8.

Schlichting, H., Gersten, K., 2017. Boundary-Layer Theory, ninth ed. Springer, Berlin, http://dx.doi.org/10.1007/978-3-662-52919-5.

Schobeiri, M.T., 2012. Turbomachinery Flow Physics and Dynamic Performance, second and enhanced ed. Springer.

Siemens PLM. Software, 2020. STAR-CCM+®, documentation version 2020 users manual.

Space Exploration Technologies Corp., 2015. Pod competition rules and requirements.

Space Exploration Technologies Corp., 2016. SpaceX Hyperloop test-track specification revision 5.

Stine, H.A., Wanlass, K., 1955. Theoretical and Experimental Investigation of Aerodynamic-Heating and Isothermal Heat-Transfer Parameters on a Hemispherical Nose with Laminar Boundary Layer at Supersonic Mach Numbers. National Advisory Committee for Aeronautics.

Sui, Y., Niu, J., Yuan, Y., Yu, Q., Cao, X., Wu, D., Yang, X., 2020. An aerothermal study of influence of blockage ratio on a supersonic tube train system. J. Therm. Stresses http://dx.doi.org/10.1007/s11630-020-1281-7.

Wang, H., Yang, Y., Coleman, D., Benedict, M., 2017. Aerodynamic simulation of high-speed capsule in the hyperloop system. In: 35th AIAA Applied Aerodynamics Conference. http://dx.doi.org/10.2514/6.2017-3741.

Wong, F., 2018. Aerodynamic design and Optimization of a Hyperloop Vehicle. Delft University of Technology.

Zhang, Y., 2012. Numerical simulation and analysis of aerodynamic drag on a subsonic train in evacuated tube transportation. J. Mod. Transp. 20 (1), 44–48. http://dx.doi.org/10.1007/bf03325776.

Zhou, K., Ding, G., Wang, Y., Niu, J., 2021. Aeroheating and aerodynamic performance of a transonic hyperloop pod with radial gap and axial channel: A contrastive study. J. Wind Eng. Ind. Aerodyn. 212, 104591. http://dx.doi.org/10.1016/j.jweia.2021.104591.

Zhou, P., Zhang, J., Li, T., Zhang, W., 2019. Numerical study on wave phenomena produced by the super high-speed evacuated tube maglev train. J. Wind Eng. Ind. Aerodyn. 190, 61–70. http://dx.doi.org/10.1016/j.jweia.2019.04.003.